Dear Author

Please use this PDF proof to check the layout of your article. If you would like any changes to be made to the layout, you can leave instructions in the online proofing interface. Making your changes directly in the online proofing interface is the quickest, easiest way to correct and submit your proof. Please note that changes made to the article in the online proofing interface will be added to the article before publication, but are not reflected in this PDF proof.

If you would prefer to submit your corrections by annotating the PDF proof, please download and submit an annotatable PDF proof by clicking here and you'll be redirected to our PDF Proofing system.

Acta Materialia xxx (2020) xxx-xxx

Contents lists available at ScienceDirect

Acta Materialia

journal homepage: www.elsevier.com/locate/actamat

Full length article

On the impact toughness of gradient-structured metals

Q1 Yan Lin[a,b,+], Qin Yu[c,+], Jie Pan[a,*], Fenghui Duan[a], Robert O. Ritchie[c,*], Yi Li[a,*]

[a] Shenyang National Laboratory for Materials Science, Institute of Metal Research, Chinese Academy of Sciences, Shenyang 110016, China
[b] University of Chinese Academy of Science, 19 Yuquan Road, Beijing, 100049, China
[c] Department of Materials Science & Engineering, University of California, Berkeley, CA 94720, United States

ARTICLE INFO

Article History:
Received 19 February 2020
Revised 14 April 2020
Accepted 14 April 2020
Available online xxx

Keywords:
Gradient structures
Grain-size gradients
Impact toughness
Dynamic *J*-R curves

ABSTRACT

Gradient-structured (GS) materials are capable of displaying high strength without compromising ductility, which can result in damage-tolerant structures. However, due to the difficulties in fabricating bulk GS materials, there has been only limited studies on the fracture behavior in GS metals. In the present work, the impact toughness of the macroscale GS pure Ni plates was investigated using instrumented Charpy impact testing. The gradient orientation was found to have a significant influence on the impact toughness of GS Ni. For gradient structures that transition from coarse grains (CG) to nano-grains (NG), termed CG→NG gradients (in the present study from ~8 μm to ~30 nm), the absorbed energy and the tensile strength were increased, respectively, by 1.6 and 2.3 times from those exhibited by uniform coarse-grained structures, demonstrating a simultaneous enhancement in strength and impact toughness. Analysis of load-displacement curves revealed that the resistance to both crack initiation and propagation were significantly enhanced as the crack penetrated through the CG→NG gradient structure, leading to markedly rising dynamic R-curve behavior estimated from nonlinear-elastic fracture mechanics *J*-based measurements. The superior fracture resistance in the CG→NG gradient structure was found to originate from sustained ductile fracture by microvoid coalescence, taking place not only in the initial CG zone, but also within the latter NG regions where adiabatic shear bands form during impact; in these latter regions, plasticity becomes enhanced due to grain coarsening induced by recrystallization under the dynamic loading. The present work not only reveals how the dynamic fracture resistance can be significantly enhanced in GS metals, but also provides structure-design strategies for developing superior metallic materials for impact engineering applications.

1. Introduction

Achieving both high strength and high toughness is a longstanding objective of materials scientists in their efforts to improve the mechanical performance of structural materials. Toughness, which can be simply considered as an integration of strength and ductility [1,2], represents the material's resistance to fracture. Nevertheless, strength and toughness tend to be mutually exclusive [1]. In many cases, high-strength metals are characterized by low ductility and inferior fracture toughness at room temperature [3–6]. For instance, for an electrodeposited nanocrystalline Ni with an ultrahigh tensile strength of over 1.57 GPa, the reported fracture toughness (K_{Ic}) is 35.5 MPa $m^{1/2}$ [6]; in contrast, the fracture toughness of the annealed coarse-grained Ni is more than six times higher (K_{Ic} ~ 220 MPa $m^{1/2}$) but with a far lower tensile strength of 340 MPa [4,7]. Similarly, the impact energy of an ultrafine-grained Grade 5 Ti alloy (grain size ~ 300 nm) with a high tensile strength of 1435 MPa is 0.15 J mm^{-2}, which is significantly lower than the impact energy (0.54 J mm^{-2}) of a coarse-grained Grade 5 Ti alloy, but this latter material displays a much lower tensile strength (965 MPa) [8]. This conflict between strength and toughness leads to an inevitable compromise for designing strong and tough structural materials [1,2].

Recently, gradient structures have attracted considerable attention. Akin to natural materials where graded structures are commonly utilized [9], gradients have been creatively engineered into novel structural materials to attain favorable combinations of mechanical properties [10–14]. It has been shown, for example, that high strength and good ductility can be simultaneously acquired in such gradient structured (GS) materials [10–12,15–17], which suggests a promising means of designing high strength, damage-tolerant materials. We hypothesize that for a nominally ductile metal, a hard phase in a GS material may act to inhibit crack initiation, whereas a softer phase may enable optimized resistance to crack propagation. Several numerical studies have been carried out to examine the influence of gradient structures on the fracture resistance. As an example, using finite element simulations, Cavaliere [18] found that, as a crack propagates from the softer region to the harder region in a GS Ni-W

* Corresponding authors.
E-mail addresses: jiepan@imr.ac.cn (J. Pan), roritchie@lbl.gov, ritchie@berkeley.edu (R.O. Ritchie), liyi@imr.ac.cn (Y. Li).
+ These authors contributed equally to this work.

https://doi.org/10.1016/j.actamat.2020.04.027
1359-6454/

alloy, the *J*-based fracture resistance increases. Moreover, molecular dynamics simulations [19] predict that a large gradient in grain size can serve as a barrier against crack propagation in nanocrystalline Ni, leading to a higher overall toughness. However, limited experimental studies have focused on the toughness of *bulk* GS materials. The lack of experimental studies on the fracture behavior of GS metals can be traced to difficulties in fabricating such gradient structures at macroscale dimensions. Early studies on many GS materials [11,12,20,21] involved section thicknesses of only a few hundred micrometers, which can rarely satisfy the size requirements for realistic fracture toughness measurement (*e.g.*, as per ASTM Standard 1820 [22]). Regardless of the technical difficulties in processing large-dimension GS metals though, there are still several unanswered questions about the toughness of such bulk materials, as to (i) experimental confirmation that the fracture toughness can actually be improved by introducing a gradient structure, and (ii) whether there is a specific effect of a grain-size gradient in resisting crack growth under both static and dynamic loading. Clearly these issues hinder a thorough understanding of toughening mechanisms in GS metals and limit their potential applications in engineering service. While our recent work has revealed the micro-mechanisms underlying the superior damage-tolerance associated with crack initiation and propagation in bulk-sized gradient nickel under quasi-static loading [23], the corresponding fracture behavior of gradient metallic materials subjected to dynamic loading has not yet to be explored. Accordingly, the objective of the present study is to investigate the influence of the gradient structure on the initiation and propagation of cracks in metals under the dynamic/impact loading conditions.

Specifically, this paper describes an experimental study to evaluate the impact toughness of gradient nickel using instrumented Charpy impact testing. By analyzing the recorded load-displacement curves obtained under impact loading, the resistance to crack initiation and propagation is quantified from the absorbed energy and the estimated dynamic crack-resistance R-curves. We systematically investigate the effect of gradients in grain size on the impact toughness of GS Ni plates. We find that coarse to nano-grained (CG→NG) gradients, with a reduction in grain size from ~8 μm to ~30 nm along the crack path, displayed an impact toughness higher than those of other gradient and monolithic-structured (MS) Ni structures. Moreover, based on nonlinear-elastic *J*-integral measurements, we observe a markedly rising dynamic R-curve for the CG→NG gradient structure, indicative of its superior damage-tolerance under impact loading. Based on microstructural characterization, we further discuss the salient toughening mechanisms underlying such crack initiation and crack propagation behavior in the CG→NG gradient Ni structure.

2. Experimental methods

2.1. Materials and test specimens

Bulk-sized gradient-structured (GS) Ni plates, with dimensions of ~40 × 60 × 2 mm^3 were fabricated by a direct-current (DC) electroplating set-up. The plating bath composition and operating conditions are described elsewhere [10]. With an increase in the current density from 10 to 100 mA/cm^2 and the additive (sodium saccharin) concentration from 1 to 5 g/L, the grain size can be continuously refined from several micrometers (~8 μm) to a few tens of nanometers (~30 nm) along the deposition direction. In order to fabricate the bulk-sized nano- to coarse-grained (NG→CG gradient) and coarse- to nano-grained (CG→NG gradient) specimens for Charpy pendulum impact testing, a ~2 mm-thick layer of monolithic nano-grained (NG) Ni (grain size ~50 nm) was further coated on the NG end and the CG end of the GS Ni plate, respectively, forming a GS plate with the final dimensions of ~40 × 60 × 4 mm^3 (Figs. 1a, b). For comparison purposes, monolithic electrodeposited nano-grained (NG) and rolled CG Ni plates were also prepared (Fig. 1d). All the GS and MS Ni plates were annealed at 393 K for 8 h to relieve any residual stresses induced by electrodeposition before subsequent specimen machining.

Miniature impact specimens with dimensions of 3 × 5 × 55 mm^3 were machined from the MS and GS Ni plates (Fig. 1c). A 45° V-notch with a depth of ~1.5 mm was machined in the 3 mm-wide specimens. The 1.5 mm-long ligament of the impact specimens, where the crack initiates and propagates, is composed of a complete gradient or monolithic structure, *i.e.* involving a CG, CG→NG, NG, or NG→CG structure, as shown in Fig. 1d. Before mechanical testing, the specimens were processed with several rounds of mechanical and electropolishing, so that smooth and residual-stress-free surfaces were prepared.

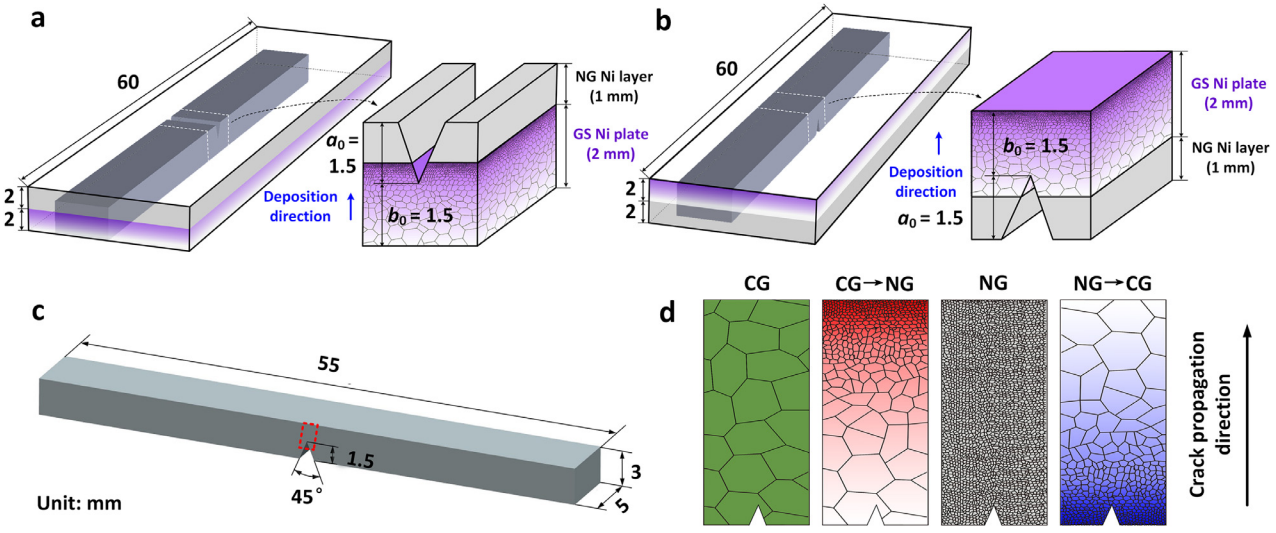

Fig. 1. Schematic diagrams illustrating the fabrication of the bulk-sized nano- to coarse-grained (NG→CG gradient) (a) and coarse- to nano-grained (CG→NG gradient) (b) impact specimens from the gradient-structured (GS) plate coated with nano-grained Ni layer. (c) The miniaturized 45 ° V-notched specimen for Charpy impact testing with the dimensions of 3 × 5 × 55 mm^3. (d) Typical grain-size gradients (~8 μm to ~30 nm) with two gradient orientations (CG→NG gradient and NG→CG gradient) and two monolithic grain structures (CG and NG) in the ligament of the specimens as circumscribed by the dashed rectangular in (c). All dimensions are in millimeters.

Please cite this article as: Y. Lin et al., On the impact toughness of gradient-structured metals, Acta Materialia (2020), https://doi.org/10.1016/j.actamat.2020.04.027

2.2. Mechanical characterization

2.2.1. Microhardness/grain-size measurements

To determine the grain-size profiles along the gradient/monolithic ligaments in the V-notched GS/MS specimens, microhardness profiles were measured across the GS/MS specimen ligaments using a Qness Q10 *A+* microhardness tester with Vickers indenter. An indentation load of 5 g was applied with a dwell time of 10 s; separation between any two neighboring indentations was ~50 μm. Grain sizes were calculated from the microhardness values using the Hall-Petch relationship [24] as follows:

$$H = 2.17\ GPa + \left(16.11\ GPa \cdot nm^{1/2}\right) d^{-1/2}, \quad (1)$$

where H is the microhardness value and d represents the grain size. The validation of determining the grain-size distribution from the microhardness profile by using Eq. (1) was checked with direct measurements by x-ray diffraction (XRD) and SEM imaging (for further information, see Fig. A.1 in the Supplementary Data in ref. [23]).

2.2.2. Quasi-static uniaxial tensile testing

To determine the quasi-static yield strength and tensile strength of the GS and MS structures, the same structured plates with a thickness of ~0.5 mm were prepared. The plates were then cut into dog-bone shaped tensile specimens, with a total length of 25 mm, a gage cross-section of 0.5×1.2 mm^2 and a gage length of 6 mm. Uniaxial tensile tests were performed on an Instron-5848 micro-tester system (Instron Corporation, Norwood, MA, USA) in ambient air, at a strain rate of $3.0 \times 10^{-4}\ s^{-1}$. Three valid tensile tests were repeated for each structured condition. Before tensile testing, all tensile specimens were electropolished to acquire a smooth, stress-free surface.

2.2.3. Instrumented Charpy impact testing

The instrumented Charpy pendulum impact testing was performed on a Zwick RKP 450 pendulum impact tester (ZwickRoell, Germany) in ambient air. The impact striker and the experimental procedure of the impact experiments were in accordance with ASTM Standard E23-18 [25]. The loading span was 40 mm. The impact speed was 5.23 m s^{-1}. At least three valid Charpy impact tests were performed on each structured condition to record the dynamic load-displacement curves.

The impact toughness of the various MS and GS structures was evaluated in terms of the total absorbed impact energy, W_{total}, *i.e.*, the total area under the load-displacement curve recorded during the impact testing (Fig. 2a). We further analyzed the absorbed impact energies associated with different stages of crack growth, *i.e.*, crack initiation, stable crack growth, unstable crack growth, and final collapse, following the methods described in refs. [27–29]. The four featured cracking stages correspond to four sections on a typical impact load-displacement curve, as schematically illustrated in Fig. 2a. The loads P_{gy}, P_{in}, P_m, P_{iu} and P_a in Fig. 2a correspond to the general yield load, the load at crack initiation, the maximum load, the load at the start of unstable crack growth, and the load at the end of unstable crack growth, respectively. The load P_{gy} corresponds to the onset of the inelastic segment of the load-displacement curve, indicating the yielding of the impact specimen. The crack initiation point, P_{in} was determined by applying the "compliance changing rate" (CCR) method [26] (for details, see Appendix A). The compliance changing rate ($\Delta C/C$) is defined as follows:

$$\Delta C/C = (C - C_{el})/C_{el}, \quad (2)$$

where $C = d\Delta/dP$ is the secant compliance (Δ and P, respectively, denote the displacement and the load), and C_{el} is the elastic compliance, which is determined as the slope (P_{el}/Δ_{el}) of the linear elastic section of the load-displacement curve (Fig. 2b). The crack initiation corresponds to the transition point at which an abrupt change in the value of $\Delta C/C$ is detected from the curve of $\Delta C/C$ *vs.* displacement (Fig. 2b). The section of unstable crack growth refers to the quasi-linear section of the load-displacement curve between P_{iu} and P_a, where a steep drop of the load is shown (Fig. 2a); the remaining section after point P_a corresponds to the final collapse stage.

2.3. Microstructure characterization

Prior to mechanical testing, the microstructures along the ligaments in the GS and MS impact specimens were characterized using an FEI Nova NanoSEM 430 scanning electronic microscope (SEM) operated at a voltage of 15 kV using a Low-kV, High-Contrast detector (vCD) in the backscattered-electron (BSE) imaging mode.

To specifically examine the crack-path profile and discern the deformation and failure mechanisms in the vicinity of the crack tip and crack wake, we electrodeposited a ~0.5 mm thick Ni layer on the exterior of the impact-tested specimens, so that the fracture surface

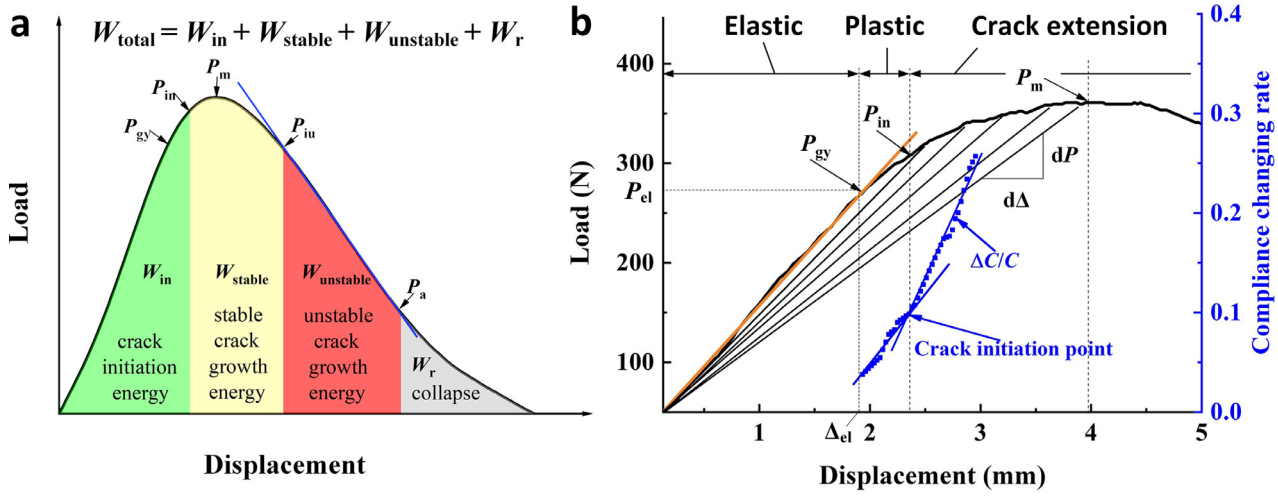

Fig. 2. (a) Schematic diagram showing the absorbed energies associated with different stages of fracture (crack initiation, stable crack growth, unstable crack growth, collapse) during an instrumented impact test. Here, P_{gy}, P_{in}, P_m, P_{iu} and P_a correspond, respectively, to the general yield load, the load at crack initiation, the maximum load, the load at the start of unstable crack growth, and the load at the end of unstable cracking. (b) Demonstration of the determination of the load at crack initiation P_{in} using the compliance changing rate (CCR) method [26]. Here, the load-displacement curve is obtained for the NG→CG gradient structure.

Please cite this article as: Y. Lin et al., On the impact toughness of gradient-structured metals, Acta Materialia (2020), https://doi.org/10.1016/j.actamat.2020.04.027

was protected. The impact-tested specimens were then sliced through the thickness at the mid-section in order to examine the deformation and fracture processes under plane-strain conditions. The interior surface of one sliced half was progressively polished to a mirror finish, followed by a final round of electropolishing. The microstructure along the crack path on the mid-plane section was imaged using FEI Nova NanoSEM 460 SEM operated at a voltage of 15 kV with a Circular Back-Scattered (CBS) detector in the BSE imaging mode. Additional microstructure characterizations using electron backscatter diffraction (EBSD) analysis were performed for the CG and NG→CG specimens to examine the impact-deformed grain structures in the plastic-wake region and in the uncracked ligament, respectively. EBSD scans for the CG specimens were conducted using an FEI Nova NanoSEM 460 SEM equipped with an Oxford EBSD detector, operating at 20 kV with a step size of 200 nm. For the NG→CG specimens, EBSD scans were conducted on a Zeiss Supra 55 microscope attached with an Oxford EBSD detector, operating at 15 kV with a step size of 50 nm.

3. Results

3.1. Microstructure of the impact specimens

BSE images taken from pure NG and pure CG structures confirmed a uniform nano-sized grain structure (Fig. 3a) and a uniform equiaxed coarse-grained structure (Fig. 3b), respectively. Based the direct measurement from the BSE images taken from the CG specimens, the average grain size of the pure CG structure was estimated to be ~50 μm. BSE images taken from the 1.5 mm-long ligaments revealed that the grain-size gradient transitions smoothly from nano-grains to coarse grains and *vice versa*, respectively, for the NG→CG and CG→NG specimens (Figs. 3c, d).

To characterize the grain size of the pure NG structure and the grain-size profiles of the GS structures, microhardness profiles were measured along the crack-propagation direction as a function of the normalized distance from 0 to 1 (0: notch tip; 1: back-end of the ligament) (Fig. 3e). The microhardness of the pure NG specimens were found to vary slightly, increasing by ~10% from ~4.5 to ~5.0 GPa along the crack-propagation direction. This microhardness variance is likely due to the slight variance of grain size caused by the degradation of the additives during the long-time electroplating. Using the Hall-Petch relationship (Eq. (1)), the average grain size of the pure NG specimens was estimated to be ~40 nm, although strictly speaking, the grain size varied from 48 nm to 32 nm from the notch tip to the back-face of the ligament.

For the NG→CG gradient specimens, the microhardness continuously decreased from ~5.1 to ~2.4 GPa as the normalized distance shifts from 0 (at the notch tip) to 1 (at the back-face of the specimen). In contrast, the microhardness for the CG→NG gradient specimens

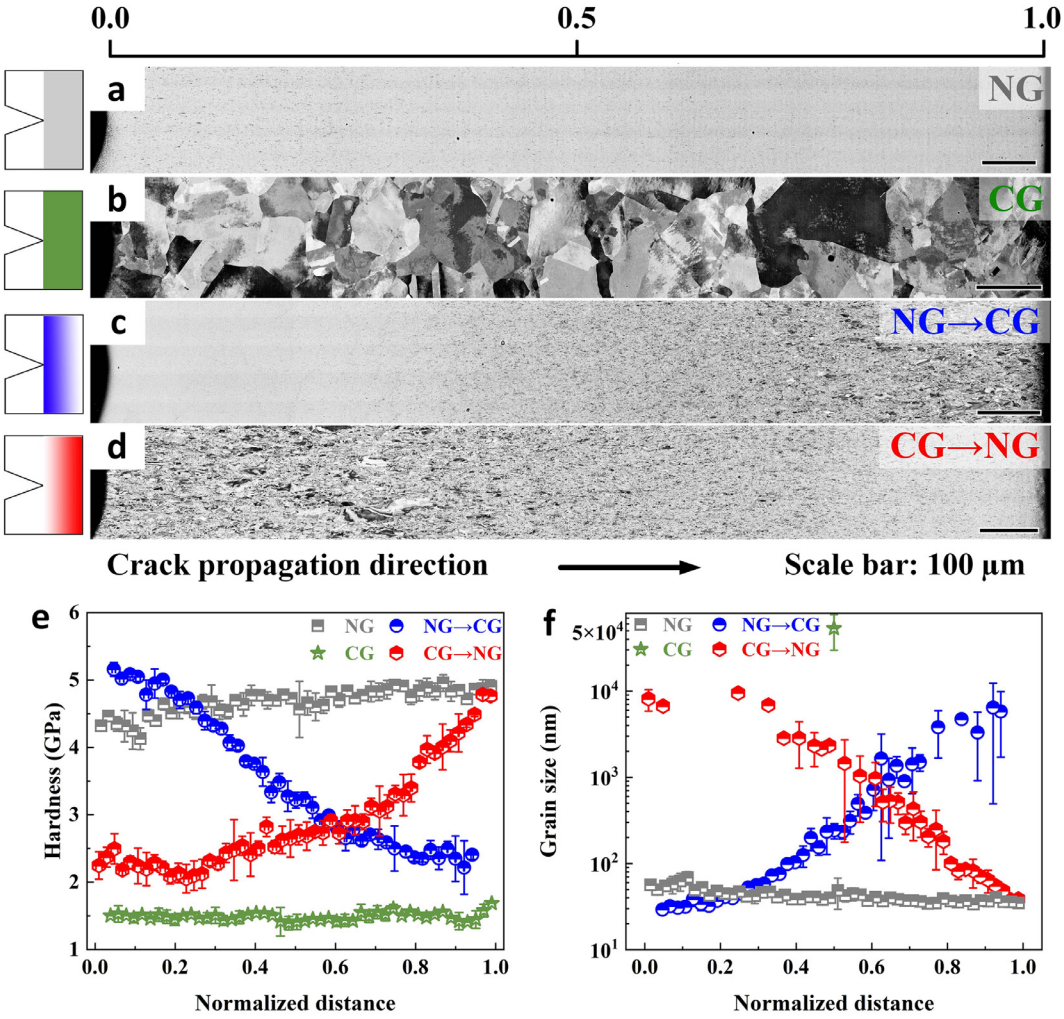

Fig. 3. Typical backscattered-electron (BSE) images taken from the ~1.5 mm-long ligament in different specimens revealing the various grain structures: (a) pure NG, (b) pure CG, (c) gradient NG→CG, and (d) gradient CG→NG, respectively. (e) Microhardness profiles measured on the ligaments of various structured impact specimens as a function of the normalized distance ranging from 0 to 1 (on the top of the figure), indicating the location ranging from the notch tip to the back-face of the specimen. (f) Grain-size distribution profiles calculated from the microhardness profiles using the Hall−Petch relationship shown in Eq. (1). Note that the grain size of the pure CG sample is measured from the BSE micrographs.

Please cite this article as: Y. Lin et al., On the impact toughness of gradient-structured metals, Acta Materialia (2020), https://doi.org/10.1016/j.actamat.2020.04.027

increased from ~2.2 to ~5.0 GPa with the increasing normalized distance. The hardness profiles of the NG→CG and CG→NG specimens are roughly symmetrical, reflecting that the profiles of their grain-size distributions are approximately identical. Using the Hall–Petch relationship (Eq. (1)), the grain size profiles for the GS specimens were calculated as a function of the normalized distance as shown in Fig. 3f. A smooth transition of the grain size from ~30 nm to ~8 μm without sharp interfaces is characterized in the NG→CG specimen whereas the CG→NG specimen exhibited approximately identical grain-size distribution but in opposite direction.

3.2. Quasi-static tensile properties

The representative engineering stress-strain curves of the gradient (CG→NG or NG→CG) and monolithic (NG and CG) structures were measured using room-temperature uniaxial tensile tests at a strain rate of $3 \times 10^{-4}\, s^{-1}$; results are presented in Fig. 4 and summarized in Table 1. Results show that the tensile strength (σ_{uts}) of the GS structure at ~760 MPa is far higher, by 126%, than that of the uniform coarse-grained CG structure (where σ_{uts} ~ 336 MPa), but much lower, by 43%, than that of the uniform nano-grained NG structure (where σ_{uts} ~ 1340 MPa). In contrast to the strength, the total elongation (ε_f) of the GS structure at ~12% is 67% smaller than that of the CG material (where ε_f ~ 37%), but ~100% larger than that of the NG material (where ε_f ~ 6%).

Results from the tensile tests show that there is a trade-off between strength and ductility in the CG and NG structures; the high-strength NG material displays brittle-like behavior with one-sixth of the ductility, whereas the ductile CG material has a factor of four lower tensile strength. However, consistent with other gradient- and heterogeneous- structured materials [10–12,30–33], the combination of strength and ductility in gradient GS materials is far superior to that in uniform-grained materials, regardless of their specific grain size. This strongly implies that the use of gradient architectures can reliably give rise to a favorable synergy of strength and damage-tolerance.

3.3. Load-displacement curves under impact loading

The load-displacement response of the impact specimens obtained from the instrumented Charpy impact tests are presented in Fig. 5. It can be seen that the impact event in the uniform NG specimens results in an initial increase in load, which then decreases rapidly as fracture ensues; a maximum load of 567 N is reached at the displacement of ~2.5 mm. This indicates that the NG structure has a strong resistance to crack initiation, but once a crack is formed, it propagates catastrophically with little resistance to crack growth. Conversely, the uniform CG specimens display a slower rising load, but only up to a maximum load of 185 N, *i.e.,* a factor of three smaller than the NG material, but at a four-fold increase in displacement of ~10 mm. Beyond the maximum load, the load drops gradually, indicating a opposite response to the NG material. Specifically, the CG Ni structure displays a much lower resistance to crack initiation than the NG Ni, but a much-improved resistance to crack growth.

Unlike the monolithic structures, it is evident from the load-displacement curves that the gradient orientation has a marked effect on the impact resistances of the metallic Ni structures. For the NG→CG specimens, the maximum load (where P_m ~ 358 N) was much lower than the 567 N for the NG specimens, presumably due to the presence of coarse grains in the specimen ligament. The subsequent rapid load drop results from rapid crack propagation which is detrimental to the toughness. With respect to the CG→NG specimens, the maximum load (where P_m ~ 362 N) was much higher than the 185 N displayed by the CG Ni specimens. Similar to the CG specimens, the post-peak load drop was relatively slow in the CG→NG specimens, suggesting more resistance to crack propagation, which is beneficial to the impact toughness.

3.4. Absorbed impact energy

The total absorbed impact energy (including both elastic and plastic contributions) for the impact tests were determined by measuring the

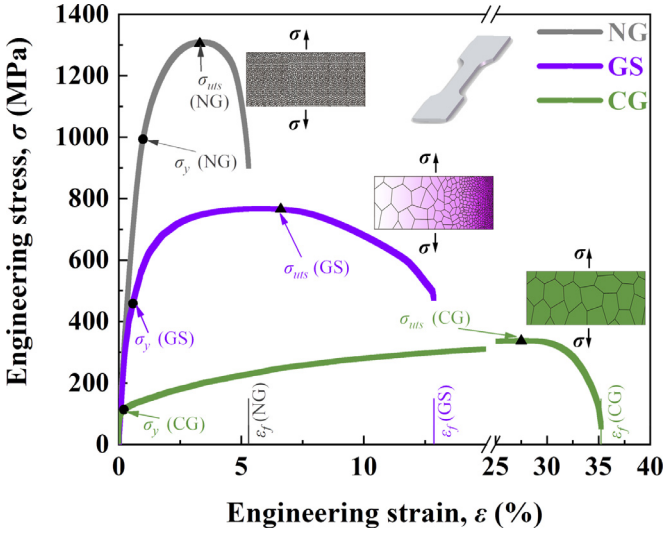

Fig. 4. Representative engineering stress-strain curves of the monolithic (CG and NG) and gradient (NG→CG or CG→NG) Ni structures, obtained at room temperature under uniaxial tension at a strain rate of $3 \times 10^{-4}\, s^{-1}$.

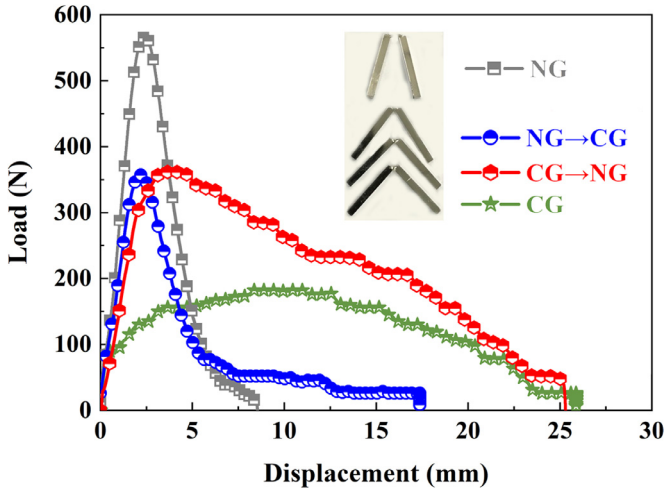

Fig. 5. Load-displacement curves for the NG, NG→CG, CG→NG, and CG V-notched specimens obtained from instrumented Charpy impact tests at room temperature. Insets show the corresponding impact-tested specimens, respectively.

Table 1
Quasi-static tensile properties of the GS and MS Ni structures at room temperature.

Specimen	Yield strength, σ_y (MPa)	Tensile strength, σ_{uts} (MPa)	Uniform elongation, ε_{ue}	Elongation to failure, ε_f
NG	936 ± 53	1341 ± 33	3.97 ± 0.32%	6.03 ± 0.62%
NG→CG or CG→NG	467 ± 14	758 ± 14	6.49 ± 0.16%	12.22 ± 0.51%
CG	119 ± 5	336 ± 2	28.05 ± 1.95%	36.58 ± 0.98%

Please cite this article as: Y. Lin et al., On the impact toughness of gradient-structured metals, Acta Materialia (2020), https://doi.org/10.1016/j.actamat.2020.04.027

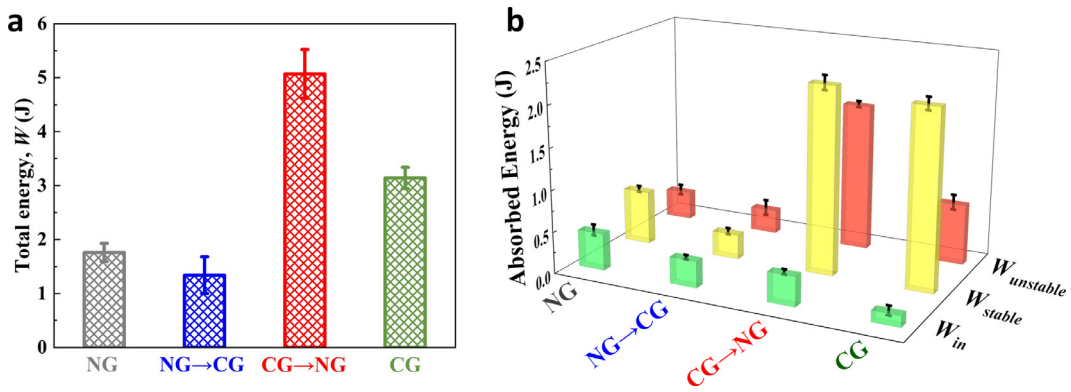

Fig. 6. (a) Total absorbed impact energy (W), and (b) absorbed impact energies associated with different stages of crack initiation W_{in}, stable growth W_{stable}, and unstable growth $W_{unstable}$, for the NG, NG→CG, CG→NG, and CG specimens, subjected to instrumented Charpy impact testing.

Table 2
The total absorbed impact energy and absorbed impact energies of various impact specimens corresponding to the different stages of fracture under dynamic loading.

Structures	W (J)	W_{in} (J)	W_{stable} (J)	$W_{unstable}$ (J)
NG	1.76 ± 0.17	0.45 ± 0.07	0.65 ± 0.04	0.34 ± 0.06
NG→CG	1.34 ± 0.34	0.32 ± 0.03	0.30 ± 0.04	0.29 ± 0.10
CG→NG	5.07 ± 0.45	0.36 ± 0.03	2.25 ± 0.09	1.77 ± 0.04
CG	3.14 ± 0.20	0.14 ± 0.06	2.16 ± 0.08	0.73 ± 0.09

total area under the load-displacement curves; these data are summarized in Fig. 6a and Table 2. The CG specimens had an impact energy of 3.14 ± 0.20 J, almost twice as that in the NG specimens, 1.76 ± 0.17 J. The impact energy of the NG→CG specimens (1.34 ± 0.34 J) was approximately at the same level as that of the NG specimens, suggesting that the impact toughness of the latter structures is not necessarily improved by creating a NG→CG gradient structure. Conversely, the CG→NG specimens exhibited a much higher total absorbed energy than the other structures. Specifically, the total absorbed energy for the CG→NG specimens (5.07 ± 0.45 J) was 1.6, 2.9 and 3.8 times higher than that measured in the CG, NG and NG→CG specimens, respectively.

One of the advantages of using instrumented Charpy impact testing is that the energies consumed during different stages of fracture, *i.e.*, crack initiation and propagation, can be separately estimated by analyzing the recorded load-displacement curves. In order to quantify the crack resistance during the different cracking stages, the absorbed energies, W_{in}, W_{stable}, and $W_{unstable}$, associated, respectively, with the stages of crack initiation, stable crack growth, and unstable crack growth, were estimated, using the CCR method [26], by finding the areas under the corresponding sections of the load-displacement curve, as schematically illustrated in Fig. 2a. Results are presented in Fig. 6b and listed in Table 2.

As shown in Fig. 6b, the NG specimens had a higher crack-initiation energy (W_{in} = 0.45 ± 0.07 J) but much reduced energies for stable (W_{stable} = 0.65 ± 0.04 J) and unstable ($W_{unstable}$ = 0.34 ± 0.06 J) crack growth, compared to those measured for the CG specimens, where W_{in} = 0.14 ± 0.06 J, W_{stable} = 2.16 ± 0.08 J and $W_{unstable}$ = 0.73 ± 0.09 J. For the NG→CG specimens, where the crack initiated on the NG side and propagated through the NG→CG gradient, the values of W_{in} (0.32 ± 0.03 J) and W_{stable} (0.30 ± 0.04 J) were only ~70% and ~46% of those in the NG specimens, respectively. As such, compared to the uniform NG material, the resistance to either crack initiation or crack propagation is not enhanced by creating the NG→CG gradient structure. Conversely, for the CG→NG specimens, where crack initiated on the CG side and propagated through the CG→NG gradient, the crack initiation energy (W_{in} = 0.36 ± 0.03 J) was increased by ~160% compared to that in the CG specimens (Fig. 6b). This result implies that the crack initiation resistance of the CG structure can be effectively enhanced by creating a coarse- to nano-grained gradient. Compared to the CG specimen, the crack propagation resistance in the CG→NG structure was also improved, which is evident by the increased values, by ~4.4% and ~143%, respectively, of the energies for stable and unstable crack propagation, compared to those for the uniform-grained CG specimens.

3.5. Plane-strain crack-path profiles

In order to understand the difference in fracture resistance of the various monolithic and gradient structures, it is necessary to discern the fracture mode as well as the associated deformation mechanisms under plane-strain conditions during crack propagation under dynamic loading. For this purpose, we sliced the impact-tested specimens through the thickness at the mid-plane section. The crack-path profiles and the deformed microstructures in the plastic-wake regions close to the crack path were examined by SEM imaging in the BSE mode. Additional microstructural characterization was performed for the gradient specimens in regions ahead of the crack tip within the uncracked ligament.

3.5.1. Nano-grained NG structures

Fig. 7 presents the crack-path profile on the mid-plane section in the fractured half for the pure NG structure. Shown is the fracture that followed a nominal mode-I crack path from the notch tip to the specimen back-face. Comparing the BSE images of the microstructure taken at the regions close to the crack path (regions C1-C3 in Fig. 7) to those taken at remote regions that are more than 1 mm away (regions R1-R3 in Fig. 7), no noticeable difference in the morphology and size of the nano-grains was detected. This indicates that the pure NG structures experienced a fine-scale brittle-like fracture during the dynamic loading.

3.5.2. Coarse-grained CG structures

In contrast to the pure NG structure, the crack-path profile at the mid-section in the statistically torn half of a pure CG specimen appeared to be more curved (Fig. 8a). Also visible are micro-voids located at the plastic-wake region close to the crack path (see the blue solid arrows in Fig. 8a). This is of typical indication that the dynamic crack propagation in the pure CG structure was driven by ductile fracture accommodated by microvoid coalescence. High-magnification BSE images (Figs. 8b,d) taken at regions C1, C3 in Fig. 8a close to the dynamic crack path clearly show the formation of distinct dislocation slip bands and sub-grain structures consisting of micro- and nano-sized dislocation cells. EBSD crystal orientation map (Fig. 8c) scanned at region C2 adjacent to region C1 in Fig. 8a near the crack path reveals that sub-grain dislocation cells form low-angle boundaries with mis-orientation angles smaller than 15° (delineated by tiny gray lines distributed discontinuously within the coarse grains in Fig. 8c). By comparison, the original coarse-grain boundaries

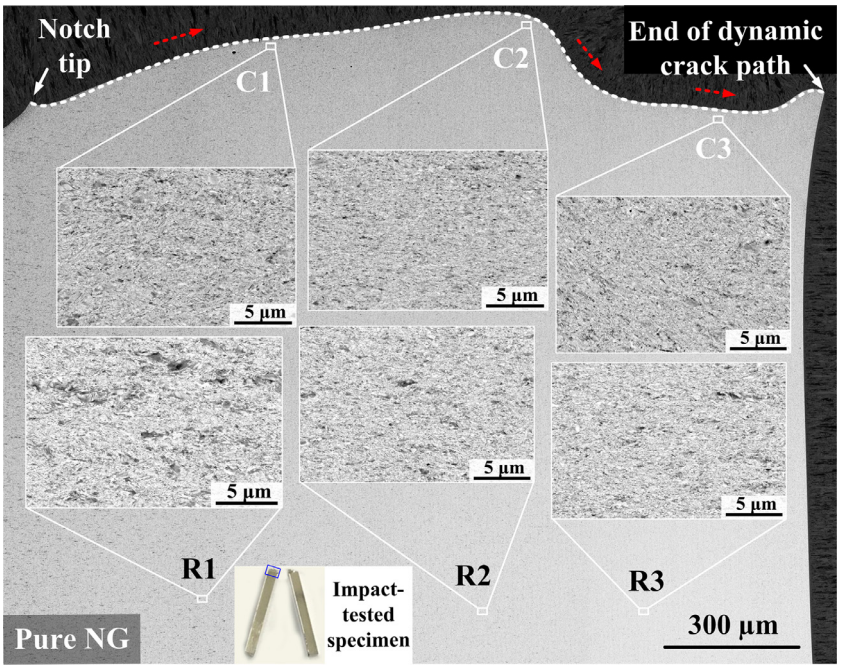

Fig. 7. Crack-path profile captured on the mid-plane section in the fractured half of a pure NG specimen. Fine-scale brittle-like fracture was seen in the pure NG structure under impact loading as evidenced by the fact that no apparent difference in the grain morphology and size was detected between the nano-grains at the regions close to the crack path (regions C1-C3) and those at remote regions more than 1 mm away (regions R1-R3). The dynamic crack-path profile is delineated in white dotted line. The propagation direction of the dynamic crack path is indicated by the red dotted arrows.

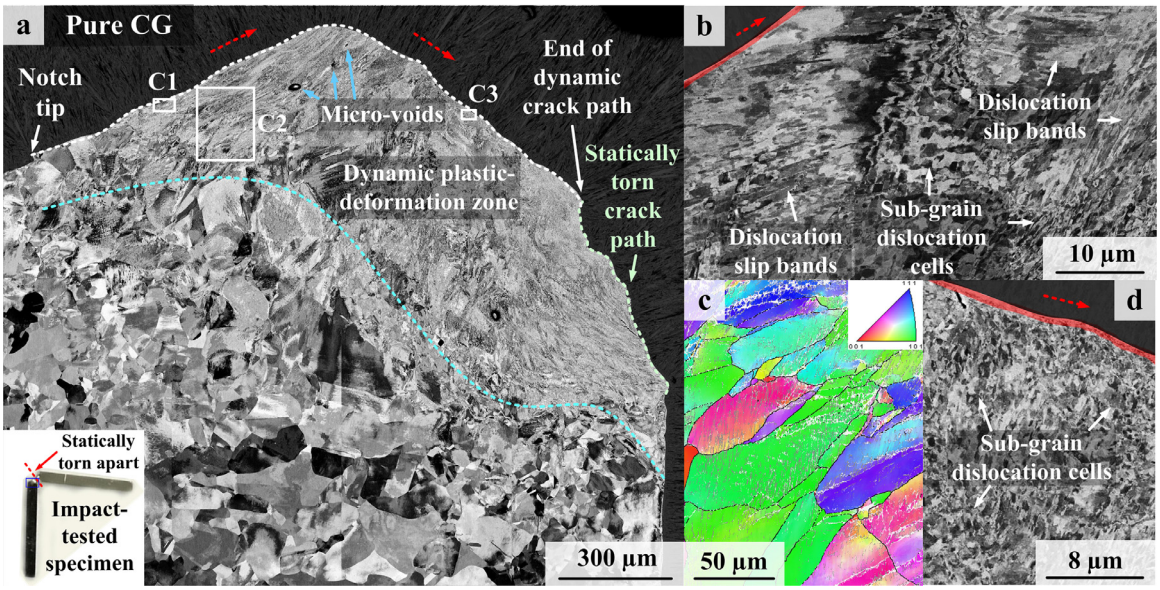

Fig. 8. Crack-path profile captured on the mid-plane section in the statically-torn half of the pure CG specimen. (a) Overall curved crack-path profile with microvoids in existence nearby (indicated by the blue solid arrows). This indicates ductile fracture by microvoid coalescence acted as the fracture mode in the pure CG structure. (b) Magnified regions C1 in (a) show the development of sub-grain structures – dislocation slip bands and dislocation cells resulting from dynamic plastic deformation. (c) EBSD crystal orientation map scanned at region C2 adjacent to region C1 in (a) near the crack path reveals sub-grain dislocation cells form low-angle boundaries (the tiny gray lines distributed discontinuously within the grain) with misorientation smaller than 15° The original coarse grain boundaries with a misorientation larger than 15° are delineated by black solid lines. (d) Magnified regions C3 in (a) indicates that the size of sub-grain dislocation cells was further refined as the crack extends to the latter half of the ligament. The dynamic crack-path profile is delineated in white dotted line in (a) and in red solid line in (b,d). The propagation direction of the dynamic crack path is denoted by the red dotted arrows.

were characterized to have misorientation angles larger than 15° (delineated by black solid lines in Fig. 8c). The refined dislocation substructures including dislocation slip bands and dislocation cells are typically a result of dynamic plastic deformation (DPD) under high strain-rate loading, consistent with the grain structures developed near the blunting edge of coarse-grained copper after Charpy impact test [34]. Moreover, along the crack-propagation direction, the average size of the sub-grain dislocation cells was reduced from ~1 μm at locations about one quarter of the crack length (region C1 in Fig. 8a, as magnified in Fig. 8b), to ~600 nm at locations of about three quarters of the crack length (region C3 in Fig. 8a, as magnified in Fig. 8d), revealing an intensified effect of sub-grain refinement associated with the dynamic crack extension. By examining whether the original coarse grains contain the sub-grained slip bands and/or dislocation cells, we can roughly estimate the depth of dynamic plastic-deformation zone (*i.e.* the distance extended from the crack path)

Please cite this article as: Y. Lin et al., On the impact toughness of gradient-structured metals, Acta Materialia (2020), https://doi.org/10.1016/j.actamat.2020.04.027

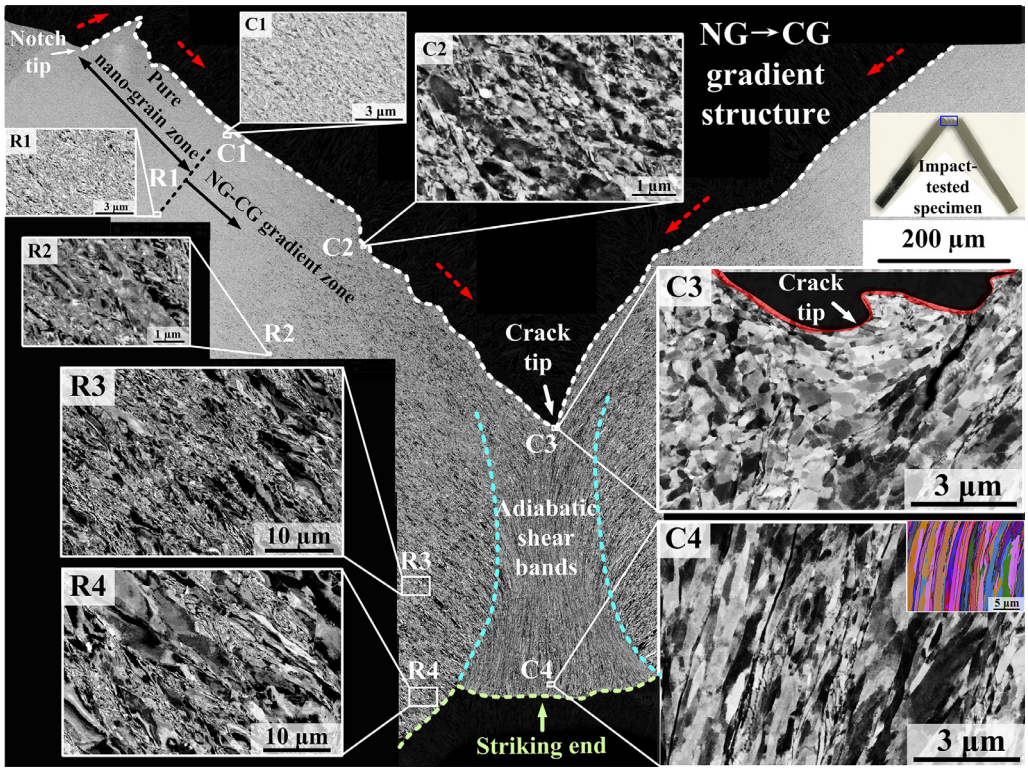

Fig. 9. Crack-path profile captured on the mid-plane section in the NG→CG gradient specimens. The brittle-like cracking mode that governed the fracture process within the initial pure nano-grain zone continues to dominate throughout the originally coarser-grained end of the NG→CG gradient zone due to the recrystallized grain refinement occurring in the adiabatic shear bands (ASBs), which are formed in the originally coarser-grained end of the NG→CG gradient zone. Regions C1-C3 reveal the microstructure resulted from dynamic plastic deformation in the plastic-wake regions along the crack path. Region C4 shows the refined lamellar structures developed in ASBs formed near the ligament end. By comparison, the representative original grain structures corresponding to the deformed microstructures in regions C1-C4 are captured in remote regions R1-R4 far away from the crack path. The dynamic crack-path profile is delineated in white dotted line. The propagation direction of the dynamic crack path is denoted by the red dotted arrows. The ASB region formed in the uncracked ligament is circumscribed by blue dotted curves. The striking end of the Charpy impact specimen is delineated by green dotted line.

being varied from approximately 150 μm (near the notch tip) to approximately 550 μm (near the crack end); this large region of local plasticity enables effective dissipation of the impact energy, which enhances resistance to crack advance, consistent with the high levels of the absorbed energy monitored during the various stages of crack propagation in the pure CG structure (Fig. 6a).

3.5.3. Gradient NG→CG structures

For the gradient structures, impact-tested NG→CG gradient specimens were significantly deformed, forming a V-shaped profile with a wide crack opening angle of ~90° (see the insect in the top right corner of Fig. 9). The entire crack path was seen to span from the notch tip, through the pure nano-grain zone and the NG→CG gradient zone, before terminating at a location roughly 70% of the total ligament length. Following crack initiation, the initial ~250 μm crack path within the nano-grain zone appeared to be straight and smooth. Comparing the deformed microstructure in region C1 in Fig. 9 to the original microstructure imaged at a region R1 remote (~120 μm away) from the fracture surface, no obvious changes in grain morphology and size could be seen, although a limited accumulation of shear bands was observed in the nano-grains close to the crack path. These features indicate that a brittle, almost cleavage-like, fracture[1] with very restricted plastic deformation dominates the initiation and early growth of the crack within the nano-grain zone. This brittle fracture mode was manifested in the low levels of the crack initiation energy for the NG→CG structure (Fig. 6b and Table 2). Once the crack entered the NG→CG gradient zone, *i.e.*, beyond region C1 (at the left half of Fig. 9), although the grain size gradually increased, the crack profile maintained a brittle-like smooth and straight appearance until the grain size exceeded ~70 nm. With subsequent extension into the NG→CG gradient zone, the brittle-like straight crack path transitioned into to a more tortuous trajectory, although a nominal mode-I fracture was still maintained.

Of note here was that microstructural changes induced by dynamic plastic deformation could clearly be identified in the plastic wake close to the crack path. Specifically, in region C2 (at the mid of Fig. 9) of the plastic-wake, where the original grain size was ~100 nm, traces of dislocation slip bands were evident; these were not in the original microstructure, as imaged in a region such as R2 remote (~220 μm away) from the crack surface. However, this dynamic plastic-deformation zone is very narrow in size, extending to a depth of only a few tens of micrometers below the crack surface, implying that energy-dissipation due to plastic deformation and its contribution to fracture resistance are still limited, even for grain sizes exceeding ~70 nm.

The dynamic crack terminated in region C3 (Fig. 9), leaving ~30% of the original ligament uncracked. A high-magnification BSE image taken from the crack tip showed abundant formation of equiaxed ultra-fine grains with average sizes in the range of ~100 to ~500 nm, although the original grain structure at this location had a columnar shape with a width of ~1 μm (see region R3 about 300 μm away from the crack tip). The transformation of the 1 μm-wide columnar grains to equiaxed ultra-fine grains is evidence of the occurrence of dynamic recrystallization of the grain structures in the vicinity of the

[1] As nickel has a face-centered cubic structure, it would not normally experience a ductile-to-brittle transition with a brittle fracture mechanism such as cleavage fracture, as is common in body-centered cubic materials, such as ferritic iron. Nickel tends to fail by microvoid coalescence at both low and high temperatures. Accordingly, the terms "brittle" and "brittle-like" are used here, not with reference to a fracture mechanism *per se*, but rather to a low-energy fracture showing little evidence, at the scale of observation, of incumbent plastic deformation, and which is characterized by a low fracture toughness.

Please cite this article as: Y. Lin et al., On the impact toughness of gradient-structured metals, Acta Materialia (2020), https://doi.org/10.1016/j.actamat.2020.04.027

crack during impact loading [35–37]. We presume that such recrystallization originated from the abrupt adiabatic increase in temperature during the impact loading as there would be insufficient time to dissipate heat converted from the work of plastic deformation during the extremely short impact loading times [34,37].

In addition to the dynamic recrystallization in the vicinity of the crack tip, adiabatic shear bands (ASBs) were visible in a 125 μm wide region in the uncracked ligament spanning all the way from the crack tip to the striking end, *i.e.*, the region bounded by blue dotted curves in Fig. 9. High-magnification BSE imaging, with an EBSD crystal orientation map, of this region (C4 in Fig. 9) clearly reveals that the shear bands were composed of elongated lamella structures with an average thickness of ~300 nm. Compared to the original coarse grains in the remote region R4 outside the ASBs (~200 μm away), the average width of the columnar-shaped grains was diminished under dynamic loading by more than an order of magnitude, from ~6 μm to ~300 nm, manifesting a significant grain refinement occurring within the ASBs. The formation of ASBs is ascribed to the strain localization during the impact loading, a phenomenon that has been commonly observed in ultra-fine grained iron and copper after high-strain-rate deformation [34,38,39]. Although the formation of ASB is a localized plastic deformation process, which may help to dissipate the impact energy, the grain refinement within the ASBs is clearly detrimental to fracture resistance. Coarse-grain structures in nickel are known to induce marked crack-tip blunting which can generate high toughness [23]; however, once they are transformed into dynamically recrystallized ultra-fine grains, the resistance to crack propagation becomes far lower. Therefore, in contrast to the crack propagation in the NG→CG gradient structure under quasi-static loading, where the growing crack was arrested as it entered the coarser-grained region of the gradient [23], under impact loading the brittle-like cracking mode that governed the fracture process within the nano-grain zone continues to dominate throughout the originally coarser-grained end of the NG→CG gradient zone due to this recrystallized grain refinement process.

The brittle-like fracture mode revealed here for the NG→CG gradient structure is also reflected in the load-displacement response of the NG→CG specimen (Fig. 5) which shows limited energy adsorption and a similar shape to that of the pure NG specimen. Moreover, as the NG→CG structure has a lower strength than the NG structure (Fig. 4 and Table 1), the maximum load achieved during the impact test was lower in the NG→CG specimens. Consequently, the NG→CG gradient structure displayed lower absorbed energies for both the crack initiation and crack propagation stages (Fig. 6b), leading to an overall energetic toughness under dynamic loading that was even lower than that of the pure NG structure (Fig. 6a).

3.5.4. Gradient CG→NG structures

Similar to the NG→CG specimen, impact-tested CG→NG specimens were bent significantly, resulting in a macroscopically V-shaped crack with a wide opening angle of ~90° (see the inset in the top right corner of Fig. 10). However, the CG→NG structure was far tougher. Unlike the overall straight crack path generated by the brittle-like fracture in the NG→CG specimen (Fig. 9), the crack-path profile at the (plane-strain) mid-section for the CG→NG specimen

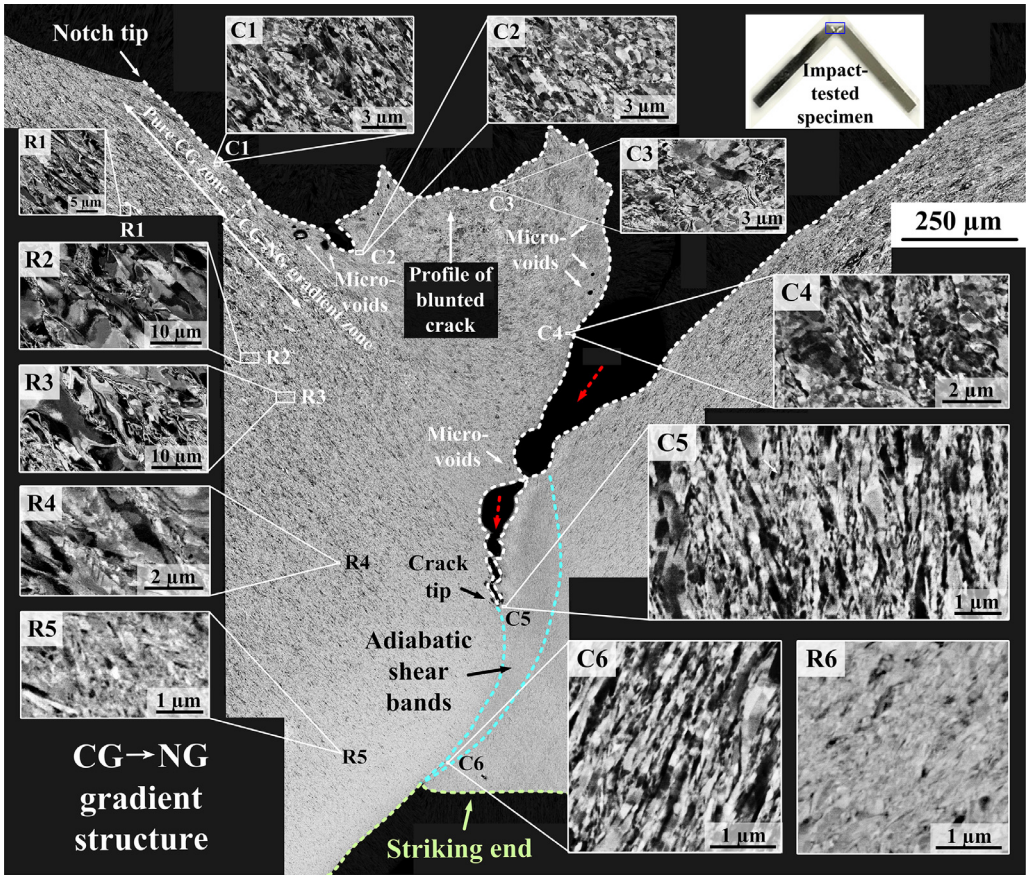

Fig. 10. Crack-path profile captured on the mid-plane section in a CG→NG gradient specimen. Ductile fracture by micro-voids coalescence that dominated the initial pure CG zone was sustained in the adiabatic shear bands (ASBs) that were formed in the latter NG zone of the CG→NG gradient. In these ASBs, plasticity was enhanced due to grain coarsening induced by dynamic recrystallization under dynamic loading. Regions C1-C5 reveal the microstructure resulting from dynamic plastic deformation in the plastic-wake regions along the crack path up to the crack tip. Region C6 shows the coarsened lamellar structures developed in the ASBs formed within the original nano-grain zone near the ligament end. By comparison, the representative original grain structures corresponding to the deformed-microstructures in regions C1-C6 are captured in remote regions R1-R6 that are far away from the crack path. The dynamic crack-path profile is delineated in white dotted lines. The propagation direction of the dynamic crack path is denoted by the red dotted arrows. The ASB region formed in the uncracked ligament is circumscribed by blue dotted curves. The striking end of the Charpy impact specimen is delineated by green dotted line.

Please cite this article as: Y. Lin et al., On the impact toughness of gradient-structured metals, Acta Materialia (2020), https://doi.org/10.1016/j.actamat.2020.04.027

revealed typical geometrical features resulting from ductile fracture (Fig. 10). Specifically, following crack initiation from the notch tip within the pure CG zone, the extending crack tip became blunted due to significant plastic deformation within the coarse-grained (~8 μm) microstructure. As shown in Fig. 10, the blunting continued until the crack formed semi-circular blunted crack tip at a region where the original grain size was ~2.5 μm (region C3 in Fig. 10). Close examination of the microstructures in regions C1-C3 near the blunted crack path revealed copious formation of dislocation slip bands, dislocation substructures and cells, which again caused substantial grain refinement in the plastic-wake regions. The depth of the impact-affected plastic zone surrounding the blunted crack profile was estimated to be as large as ~300 μm, which significantly contributes to the high levels of absorbed energy during the stages of crack initiation and stable crack growth in this gradient structure (Fig. 6b and Table 2).

When the crack propagated further into the gradient CG→NG zone, microvoids nucleated and coalesced, leading to the initial development of a mode-I crack path, as shown in region C2 as well as the main crack path subsequent to the blunted profile in Fig. 10. However, once the crack proceeded into regions of the gradient where the grain size decreased to below ~1 μm, the prior mode-I crack path was no longer sustained and instead followed a distinctly curved trajectory. Repeatedly, microvoids were formed in the plastic-wake regions along the crack path indicative of crack extension by microvoid coalescence associated with extensive plastic deformation (*e.g.,* in region C4 in Fig. 10). The curved cracking eventually terminated in the nano-grained zone of the gradient where the original grain size was ~80 nm, leaving a 400-μm uncracked ligament. Immediately ahead of the arrested crack tip, in region C5 in Fig. 10, a lamella grain structure elongated in the direction of the crack path was developed. Compared to the ~80 nm width of the original columnar grains at this location, the width of the elongated grains varied from 100 to 800 nm, clearly showing dynamic grain coarsening had occurred in this region. Within this narrow deformation region, which extended from the crack tip to the bottom (impacted) surface of the specimen (bounded by blue dotted curves in Fig. 10), there was evidence of abundant adiabatic shear bands. However, unlike the dislocation substructures that formed in the initial pure CG zone, this latter region of the CG→NG gradient structure comprised fine lamella-shaped grains, several micrometers in length sized with a thickness that varied between ~50 to 300 nm (see region C6 in Fig. 10).

The coarsening of the nano-grains and associated formation of ASBs near the end of the CG→NG gradient zone can again be attributed to dynamic recrystallization during the impact loading. Such grain coarsening in the ASBs leads to structural softening which can promote plasticity in the otherwise high-strength nano-grained region [11,40]. Thus, unlike the pure NG structure where cracking proceeded by a brittle-like mode, the enhanced plasticity associated with the coarsening of the nano-grain zone in the CG→NG gradient acts to preserve a ductile mode of crack advance. This led to the load-displacement response of the CG→NG specimen showing a prolonged softening tail, with a total displacement similar to that of the pure CG specimen (Fig. 5). Moreover, as the tensile strength of the CG→NG structure is ~30% higher than that of the pure CG structure (Fig. 4), the maximum load achieved during impact loading was also correspondingly higher by ~100%. The result is that CG-NG gradient structure displays by far best crack resistance to impact loading over all the other monolithic and gradient structures, with a higher impact energy coupled with a tensile strength exceeding 750 MPa.

4. Discussion

4.1. Estimation of the dynamic J-R curve

To further evaluate the fracture resistances of the gradient- and monolithic- structured Ni under the impact loading, we estimated the nonlinear-elastic fracture-mechanics-based dynamic *J*-R curves from the load-displacement data following the key curve method [41,42]; the resulting crack-resistance curves are shown in Fig. 11. Details of the key curve method are described in Appendix A.

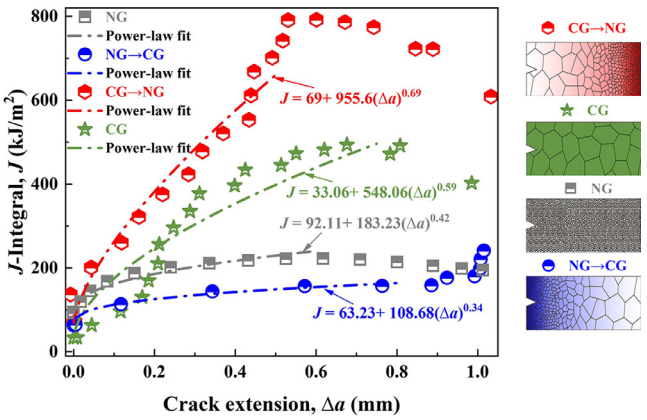

Fig. 11. Dynamic *J*-R curves, showing the variation in the value of *J* to sustain crack extension Δa, for the studied monolithic and gradient Ni structures under impact loading. The R-curves are estimated from the load-displacement data (Fig. 5) using the key curve method [41,42]. Interestingly, dependent on the direction of crack growth with respect to the gradient in grain size, the gradient structures display the best (for the CG→NG gradient) and the worst (for the NG→CG gradient) of the Ni structures evaluated.

During the initial stages of crack growth (Δa < ~0.2 mm), the NG→CG gradient structure, akin to the two monolithic NG and CG structures, required a low applied *J*-value to instigate and sustain cracking. In contrast, the corresponding applied *J* to sustain initial cracking (Δa < ~0.2 mm) in the CG→NG gradient specimen was roughly two times higher than those in the uniform coarse-grain CG and NG→CG specimens. As the crack further extended (in excess of Δa ~ 0.2 mm), the dynamic *J*-R-curves of the CG→NG and CG specimens rose very steeply. The R-curves for the CG→NG gradient structure maintained the highest crack resistance of all the Ni structures tested. By comparison, the uniform-grained NG and the NG→CG gradient specimens, displayed only marginally rising R-curves with crack extension, a characteristic that is indicative of low resistance to crack propagation and hence inferior damage-tolerance.

The rising *J*-R curves for all the structures terminated as the crack extended to ~0.6 mm, after which the R-curves (except for the lowest NG→CG R-curve) started to drop. The maximum *J*-integral value achieved in the CG→NG gradient specimen was ~800 kJ/m^2, which is roughly 1.6 times as that in ductile CG specimen and 3 times higher than those in the NG and the NG→CG gradient specimen.

The dynamic *J*-R curves results presented in Fig. 11 confirm that the impact toughness has a strong dependency on the gradient orientation in GS Ni. Negligible toughening is observed in the NG→CG gradient structure as revealed by the insignificant-rising dynamic *J*-R curve, implying a typical brittle fracture behavior akin to the pure NG structure. However, the CG→NG gradient structure displays an exceptional rising *J*-R curve, suggesting a dynamic fracture toughness superior to all the investigated GS and MS structures.

4.2. Extraordinary strength-impact toughness synergy in gradient-grained structures

For conventional structural materials, there is invariably an unavoidable trade-off between strength and fracture toughness, which is clearly demonstrated by the Ashby map where the yield strength *vs.* the fracture toughness are plotted [43]. As in nature, one approach to solving this strength-toughness "conflict" is through the use of gradient-grained architectures [9]. In line with this, we have successfully synthesized bulk GS-Ni structures possessing a gradient in grain size in two configurations (*i.e.*, NG→CG gradient and CG→NG gradient). Our earlier work has revealed that the best combination of

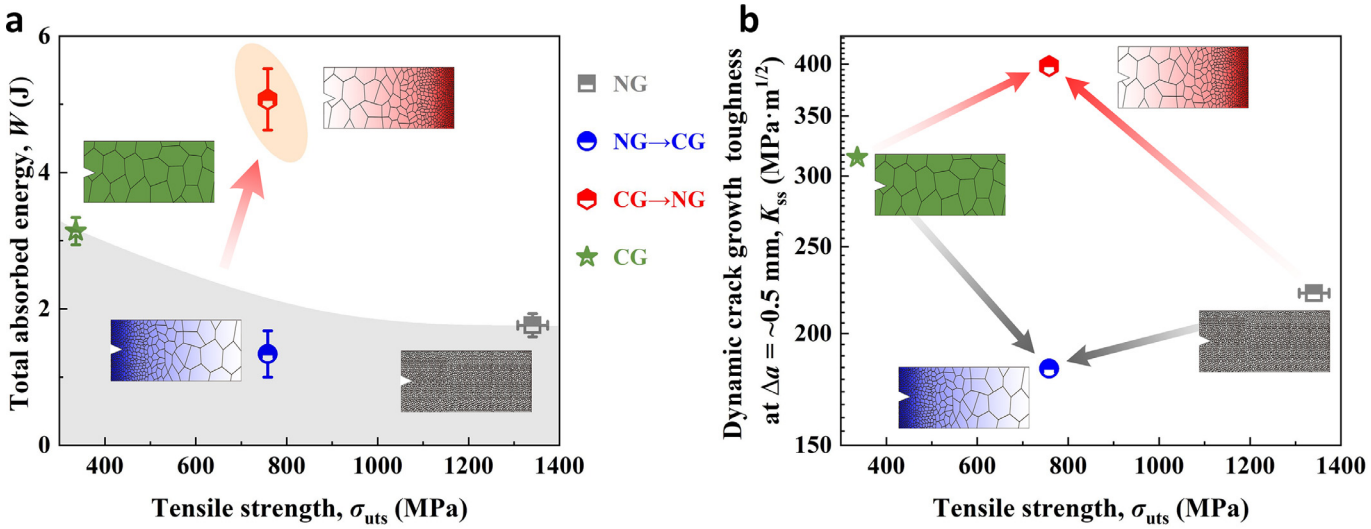

Fig. 12. Strength *vs.* impact toughness. (a) Plot showing the total absorbed impact energy as a function of the quasi-static tensile strength, (b) Ashby map showing the approximate dynamic crack-growth toughness K_{ss} at $\Delta a \sim 0.5$ mm as a function of the quasi-static tensile strength for the GS and MS structures; here, $K_{ss} = (E'J)^{1}/_{2}$, $E' = E/(1-\nu^2)$. For pure Ni, E and ν are 200 GPa and 0.312, respectively.

strength and toughness properties can be achieved under the static loading with a coarse- to fine-grained (CG→NG) gradient structures [23]. Here, we extend this approach to examine whether the strength-toughness synergy still prevails with such gradient structures under impact/dynamic loading conditions.

The impact toughness of the GS and MS structures are plotted in Fig. 12 as a function of their tensile strengths. Two measurements of the impact toughness are utilized, *i.e.,* a global measure using the total absorbed impact energy (W) (Fig. 12a), and a nonlinear-elastic fracture-mechanics-based estimate of the dynamic crack-growth toughness (K_{ss}) at $\Delta a \sim 0.5$ mm (Fig. 12b). (Note that the method used to convert the estimated J-based crack-growth toughness values into approximate K-based values is described in the Appendix A). As presented in Fig. 12a, there exists a trade-off between the strength and the total absorbed impact energy for the CG, NG, and NG→CG gradient structures, as shown by the light gray zone in Fig. 12a. Specifically, although the CG specimens have the lowest tensile strength, the total absorbed impact energy of the CG specimens is almost ~80% higher than those of the NG→CG gradient and the NG specimens. However, this issue of the generally mutually exclusive properties of strength and toughness can be alleviated with a coarse- to nano-grained (CG→NG) gradient structure which, compared to the uniform CG material, displays simultaneous increases in tensile strength and total absorbed impact energy by, respectively, 125% and 60% (as shown by the red data point above the midst of the light gray zone in Fig. 12a). Indeed, the CG→NG structure is clearly superior to the pure NG and even NG→CG gradient structures, as shown in Fig. 12b. *The fascinating consequence of this is that although gradient grain-sized structures can combine the high strength of the nano-grained structures and the far higher toughness of the coarser-grained ones, this is only the case under impact loading if the crack grows in the general direction of a coarse-to-fine grained gradient, i.e., for the present Ni CG→NG structure, due to the beneficial effects of nano-grain coarsening by dynamic recrystallization.*

4.3. Gradient-orientation-dependent impact toughness: implication for engineering applications

The fracture resistance to the impact loading in the gradient structured materials is strongly dependent on the gradient orientation. As clearly observed in Fig. 12b, the crack-growth toughness (K_{ss}) (398 MPa·m$^{1/2}$) at $\Delta a \sim 0.5$ mm of the CG→NG structure far surpasses that (183 MPa·m$^{1/2}$) in the NG→CG structure.[2] This finding is consistent with the difference of the absorbed impact energies during the various stages of fracture. For ductile materials subjected to impact loading, the absorbed energy for crack growth ($W_{stable} + W_{unstable}$), rather than that for crack initiation (W_{in}), contributes to most of the total absorbed energy. Accordingly, the impact toughness is more likely to be associated with the resistance to crack growth rather than the resistance to crack initiation during the impact loading. As revealed in our study, the values of W_{stable} and $W_{unstable}$ in the NG→CG specimens are considerably lower than those in the CG→NG specimens (Fig. 6b), representative of the fact that the impact resistance of the CG→NG gradient structure is far superior to that of the NG→CG gradient structure.

With respect to the material structure design for engineering application, our current findings suggest that create fine- to coarse-grained gradient architectures may not be optimal for a material's impact toughness, although we have not found such behavior under quasi-static loading conditions [23]. Actually, under the quasi-static loading, the slope of the quasi-static J-R curve keeps rising as the crack grows from the NG region to the CG region, indicating an enhanced crack-growth toughness. Therefore, the NG→CG gradient structure might be preferred for certain safety-critical applications under the quasi-statistic loading conditions, but should be avoided in applications that involve high strain-rate loading.

On the other hand, as shown in Fig. 12b, the crack-growth toughness of the CG→NG specimens are much higher than the NG→CG specimens and even surpass that of the CG specimens. This indicates that the CG→NG gradient structure is more suited for dynamic loading conditions. As confirmed from the analysis of the absorbed energies (Fig. 6), the CG→NG gradient structure significantly increases the absorbed energies for both crack initiation and unstable growth, without losing resistance to the stable crack growth. In short, coarse- to fine-grained gradient structures present distinct advantages over

[2] For K_{SS} (or J_{SS}) to be considered as a size-independent fracture toughness value, the validity requirements for the J-field dominance and plane-strain conditions should be met [22], *i.e.*, that b_0, $B > \frac{10J_{SS}}{\sigma_0} = \frac{10K_{SS}{}^2/\left(E/(1-\nu^2)\right)}{\sigma_0}$, where σ_0 is the flow strength (average of yield strength and tensile strength). b_0 and B are the initial ligament length and specimen thickness, respectively. The K_{SS} values measured for the NG, NG→CG, NG→CG, and CG specimens (Fig. 12b) are 222 MPa·m$^{1/2}$, 183 MPa·m$^{1/2}$, 398 MPa·m$^{1/2}$, and 315 MPa·m$^{1/2}$, respectively. As all of these values do not satisfy the ASTM requirements for J-dominance at the crack tip, these values are not strictly ASTM valid [22].

uniform grained structures in terms of their superior damage-tolerance as structural materials for applications involving high-strain-rate impact loading conditions.

5. Conclusions

Based on an experimental study of the effects of grain-size gradients on the strength and dynamic fracture resistance of bulk nickel plates, the following conclusions can be made:

1. Using gradients in grain size, synthesized by direct current electrodeposition, from nano-sized grains of ~30 nm (NG) to coarser grains of ~8 μm (CG), the impact toughness of the gradient-structured (GS) Ni, assessed using instrumented Charpy impact testing, was compared to that of uniform grain-sized nano-grained (NG) and coarse-grained (CG) structures. Gradient orientation was found to significantly affect the impact toughness. Test specimens with an NG→CG gradient structure displayed a relatively low fracture resistance to impact loading, similar to that exhibited by the nominally brittle uniform nano-grained (NG) specimens. Conversely, although the tensile strength of the gradient structures was 43% lower than that of the NG structures, the CG→NG gradient structure displayed a strength and impact energy that was over ~2.0 and ~1.5 times higher than those of the CG structure. Indeed, the CG→NG gradient structure was definitively the most damage-tolerant Ni structure representing the best combination of strength and impact toughness.
2. The superior dynamic fracture resistance of the CG→NG gradient structure was ascribed to the sustained ductile fracture by microvoid coalescence, which was active not only in the initial coarse-grained region, but also in the adiabatic shear bands formed in the subsequent nano-grained region, as plasticity was enhanced in the latter region due to the grain coarsening induced by dynamic recrystallization under the impact loads.
3. This work presents a novel strategy of using coarse- to nano-grained gradient structures in order to design strong, tough and hence damage-tolerant metallic structures for engineering applications involving high-strain rate/impact loading.

Acknowledgments

This work was financially supported by National Key Research and Development Program of China (No. 2017YFB0702003) and by National Natural Science Foundation of China under grant Nos. 51471165 and 51871217 for Y.L., J.P., F.H.D. and Y.L. R.O.R. acknowledges support from the H.T. and Jessie Chua Distinguished Professorship at Berkeley.

Supplementary materials

Supplementary material associated with this article can be found in the online version at doi:10.1016/j.actamat.2020.04.027.

Appendix A. Estimation of dynamic *J*-R curves

The nonlinear-elastic fracture-mechanics-based *J*-integral resistance curve (*i.e.*, the *J*-R curve) is commonly used to describe the fracture resistance as a function of crack extension [22,37]. Due to its effectiveness in characterizing both the crack-initiation and crack-growth toughnesses of ductile materials, the *J*-integral and *J*-R curve have become important material parameters in the evaluation of the damage-tolerance of structural materials. As these parameters can be similarly utilized at high loading rates, the pre-cracked impact specimens can be utilized to determine the dynamic *J*-R curve from the recorded load-displacement curves using the instrumented Charpy impact testing [26]. For the notched impact specimens without fatigue pre-cracking, which were used in our current study, prior work has shown that the dynamic *J*-R curve can still be estimated using the so-called "key curve" method [41,42].[3]

Based on this method, the load-displacement curve between P_{gy} (load at yield) and P_{in} (load at crack initiation) can be fitted by the following power law:

$$\frac{PW}{b_0^2} = k\left(\frac{\Delta_{pl}}{W}\right)^m, \tag{A1}$$

where P and W denote the load and the specimen width (~3 mm), respectively; a_0 (~1.5 mm) and $b_0 = (W - a_0)$ are the initial crack length (equal to the notch depth in this work) and the initial ligament length, respectively. $\Delta_{pl} = \Delta - C_{el} P$ refers to the displacement due to plastic deformation, where Δ is the instant displacement while C_{el} is the elastic compliance, determined as the slope (P_{el}/Δ_{el}) of the linear elastic section of the load-displacement curve. Once the dimensionless constants k and m are determined, Eq. (A1) can be applied to derive the remaining ligament length (b) from the load-displacement curve beyond the crack initiation point using following relationship [41]:

$$\frac{PW}{b^2} = k\left(\frac{\Delta_{pl}}{W}\right)^m, \tag{A2}$$

Accordingly, the crack extension Δa at each point after crack initiation can be derived:

$$\Delta a = b_0 - b = W - a_0 - b = (W - a_0) - \sqrt{\frac{PW^{m+1}}{k(\Delta_{pl})^m}} \tag{A3}$$

The dynamic *J*-integral value can then be calculated from the relationship for pure bending proposed by Rice and coworkers [44]:

$$J = \frac{\eta U}{B(W - a_0)}, \tag{A4}$$

where B is the specimen thickness (~5 mm), U is the potential energy during the impact testing, which equals to the total absorbed energy determined by finding the total area under the load-displacement curve. The value of η was taken as 2 for pre-cracked and 1.46 for Charpy V-notch specimen [45]. Considering the effect of crack growth on the *J*-integral, the Garwood's formula [46] to correct the dynamic *J*-integral values for the three-point bend specimen was used:

$$J_n = J_{n-1}\frac{W - a_n}{W - a_{n-1}} + \frac{\eta U_n}{B(W - a_{n-1})}, \tag{A5}$$

where U_n refers to the area under the actual test record between deflection Δ_n and Δ_{n-1}. By following Eqs. (A1) to (A5), we can construct the dynamic *J*-R(Δa) curve by calculating the *J*-integral corresponding to the specific crack extensions (Δa) on the basis of the recorded load-displacement/deflection curve. The off-set power law was used to fit the dynamic *J*-R curves at the stage of stable crack growth [45]:

$$J = m + l(\Delta a)^n, \tag{A6}$$

where m, l, and n are fitting parameters.

Approximate stress intensity *K*-based toughness values were back-calculated from the *J* values using the standard mode-I *J*-*K* equivalence relationship:

$$J = K^2/E', \tag{A7}$$

[3] The *J*-integral, like other characterizing parameters in fracture mechanics such as the stress intensity factor *K*, were originally derived for homogeneous isotropic continua [47]. However, they have been widely used, indeed mostly used, to examine materials and microstructures where such homogeneity is difficult to rationalize. The underlying justification for using such fracture mechanics analyses is that the structural size-scales remain small compared to the extent of the *J*-dominated (or *K*-dominated) crack-tip stress and displacement fields, and that this in turn remains small compared to the macroscale of the test sample.

where is $E' = E / (1- \nu^2)$ for plane-strain conditions; E is Young modulus and ν is Poisson's ratio.

For the purposes of comparison of the effective fracture toughnesses of the various monolithc and gradient Ni structures in Fig. 12, a crack-growth toughness for dynamic loading, K_{ss}, was calculated as the approximate K values for a crack-extension of $\Delta a = 0.5$ mm.

References

[1] R.O. Ritchie, The conflicts between strength and toughness, Nat. Mater. 10 (2011) 817–822, doi: 10.1038/nmat3115.
[2] M.E. Launey, R.O. Ritchie, On the fracture toughness of advanced materials, Adv. Mater. 21 (2009) 2103–2110, doi: 10.1002/adma.200803322.
[3] I.A. Ovid'ko, R.Z. Valiev, Y.T. Zhu, Review on superior strength and enhanced ductility of metallic nanomaterials, Prog. Mater. Sci. 94 (2018) 462–540, doi: 10.1016/j.pmatsci.2018.02.002.
[4] A. Hohenwarter, R. Pippan, Fracture toughness evaluation of ultrafine-grained nickel, Scr. Mater. 64 (2011) 982–985, doi: 10.1016/j.scriptamat.2011.02.007.
[5] M.C. Jo, J. Park, S.S. Sohn, S. Kim, J. Oh, S. Lee, Effects of untransformed ferrite on Charpy impact toughness in 1.8-GPa-grade hot-press-forming steel sheets, Mater. Sci. Eng. A. 707 (2017) 65–72, doi: 10.1016/j.msea.2017.09.027.
[6] R.A. Mirshams, C.H. Xiao, S.H. Whang, W.M. Yin, R-Curve characterization of the fracture toughness of nanocrystalline nickel thin sheets, Mater. Sci. Eng. A. 315 (2001) 21–27, doi: 10.1016/S0921-5093(01)01213-8.
[7] M. Srinivas, G. Malakondaiah, P.R. Rao, Fracture toughness of f.c.c. nickel and strain ageing b.c.c. iron in the temperature range 77–773 K, Acta Metall. Mater. 41 (1993) 1301–1312, doi: 10.1016/0956-7151(93)90181-Q.
[8] I.P. Semenova, A.V. Polyakov, V.V. Polyakova, Y.F. Grishina, Y. Huang, R.Z. Valiev, T.G. Langdon, Mechanical behavior and impact toughness of the ultrafine-grained Grade 5 Ti alloy processed by ECAP, Mater. Sci. Eng. A. 696 (2017) 166–173, doi: 10.1016/j.msea.2017.04.073.
[9] Z. Liu, M.A. Meyers, Z. Zhang, R.O. Ritchie, Functional gradients and heterogeneities in biological materials: design principles, functions, and bioinspired applications, Prog. Mater. Sci. (2017), doi: 10.1016/j.pmatsci.2017.04.013.
[10] Y. Lin, J. Pan, H.F. Zhou, H.J. Gao, Y. Li, Mechanical properties and optimal grain size distribution profile of gradient grained nickel, Acta Mater. 153 (2018) 279–289, doi: 10.1016/j.actamat.2018.04.065.
[11] T.H. Fang, W.L. Li, N.R. Tao, K. Lu, Revealing extraordinary intrinsic tensile plasticity in gradient nano-grained copper, Science 331 (2011) 1587–1590, doi: 10.1126/science.1200177.
[12] X. Wu, P. Jiang, L. Chen, F. Yuan, Y.T. Zhu, Extraordinary strain hardening by gradient structure, Proc. Natl. Acad. Sci. 111 (2014) 7197–7201, doi: 10.1073/pnas.1324069111.
[13] R. Thevamaran, O. Lawal, S. Yazdi, S.-J. Jeon, J.-H. Lee, E.L. Thomas, Dynamic creation and evolution of gradient nanostructure in single-crystal metallic microcubes, Science (80-.). 354 (2016) 312–316, doi: 10.1126/science.aag1768.
[14] D. Kokkinis, F. Bouville, A.R. Studart, 3D printing of materials with tunable failure via bioinspired mechanical gradients, Adv. Mater. 30 (2018) 1705808, doi: 10.1002/adma.201705808.
[15] K. Lu, Making strong nanomaterials ductile with gradients, Science 345 (2014) 1455–1456 (80-.), doi: 10.1126/science.1255940.
[16] Z. Zeng, X. Li, D. Xu, L. Lu, H. Gao, T. Zhu, Gradient plasticity in gradient nano-grained metals, Extrem. Mech. Lett. 8 (2016) 213–219, doi: 10.1016/j.eml.2015.12.005.
[17] X.L. Wu, P. Jiang, L. Chen, J.F. Zhang, F.P. Yuan, Y.T. Zhu, Synergetic strengthening by gradient structure, Mater. Res. Lett. 2 (2014) 185–191, doi: 10.1080/21663831.2014.935821.
[18] P. Cavaliere, Crack tip plasticity in plastically graded Ni–W electrodeposited nanocrystalline alloys, Comput. Mater. Sci. 41 (2008) 440–449, doi: 10.1016/j.commatsci.2007.05.007.
[19] P. Wang, X. Yang, X. Tian, Fracture behavior of precracked nanocrystalline materials with grain size gradients, J. Mater. Res. 30 (2015) 709–716, doi: 10.1557/jmr.2015.18.
[20] J. Long, Q. Pan, N. Tao, M. Dao, S. Suresh, L. Lu, Improved fatigue resistance of gradient nanograined Cu, Acta Mater. 166 (2019) 56–66, doi: 10.1016/j.actamat.2018.12.018.
[21] L. Yang, N.R. Tao, K. Lu, L. Lu, Enhanced fatigue resistance of Cu with a gradient nanograined surface layer, Scr. Mater. 68 (2013) 801–804, doi: 10.1016/j.scriptamat.2013.01.031.
[22] ASTM E1820-17a, Standard test method for measurement of fracture toughness, Annual Book of Standards 44 (2013) 1–54.
[23] R. Cao, Q. Yu, J. Pan, Y. Lin, A. Sweet, Y. Li, R.O. Ritchie, On the exceptional damage-tolerance of gradient metallic materials, Mater. Today 32 (2020) 94–107, doi: 10.1016/j.mattod.2019.09.023.
[24] Y. Lin, J. Pan, Z. Luo, Y. Lu, K. Lu, Y. Li, A grain-size-dependent structure evolution in gradient-structured (GS) Ni under tension, Nano Mater. Sci. (2019), doi: 10.1016/j.nanoms.2019.12.004.
[25] ASTM E23-18, Standard methods for notched bar impact testing of metallic materials, Annual Book of Standards (2005) 1–26.
[26] D. Petersen, T. Kobayashi, I. Yamamoto, M. Niinomi, Introduction of a new dynamic fracture toughness evaluation system, J. Test. Eval. 21 (1993) 145, doi: 10.1520/JTE11763J.
[27] International Standard ISO 14556:2015(E). Metallic Materials—Charpy V-notch Pendulum Impact Test—Instrumented Test Method, 2nd Ed.
[28] N.D. Alexopoulos, A. Stylianos, Impact mechanical behaviour of Al–7Si–Mg (A357) cast aluminum alloy. the effect of artificial aging, Mater. Sci. Eng. A. 528 (2011) 6303–6312, doi: 10.1016/j.msea.2011.04.086.
[29] N.D. Alexopoulos, A. Stylianos, J. Campbell, Dynamic fracture toughness of Al-7Si-Mg (A357) aluminum alloy, Mech. Mater. 58 (2013) 55–68, doi: 10.1016/j.mechmat.2012.11.005.
[30] X. Wu, M. Yang, F. Yuan, G. Wu, Y. Wei, X. Huang, Y. Zhu, Heterogeneous lamella structure unites ultrafine-grain strength with coarse-grain ductility, Proc. Natl. Acad. Sci. 112 (2015) 14501–14505, doi: 10.1073/pnas.1517193112.
[31] Y. Wei, Y. Li, L. Zhu, Y. Liu, X. Lei, G. Wang, Y. Wu, Z. Mi, J. Liu, H. Wang, H. Gao, Evading the strength-ductility trade-off dilemma in steel through gradient hierarchical nanotwins, Nat. Commun. 5 (2014) 1–8, doi: 10.1038/ncomms4580.
[32] Z. Cheng, H. Zhou, Q. Lu, H. Gao, L. Lu, Extra strengthening and work hardening in gradient nanotwinned metals, Science 362 (2018) eaau1925 (80-.)., doi: 10.1126/science.aau1925.
[33] C.X. Huang, Y.F. Wang, X.L. Ma, S. Yin, H.W. Höppel, M. Göken, X.L. Wu, H.J. Gao, Y.T. Zhu, Interface affected zone for optimal strength and ductility in heterogeneous laminate, Mater. Today 21 (2018) 713–719, doi: 10.1016/j.mattod.2018.03.006.
[34] N. Liang, Y. Zhao, J. Wang, Y. Zhu, Effect of grain structure on Charpy impact behavior of copper, Sci. Rep. 7 (2017) 44783, doi: 10.1038/srep44783.
[35] A. Mishra, B. Kad, F. Gregori, M. Meyers, Microstructural evolution in copper subjected to severe plastic deformation: experiments and analysis, Acta Mater. 55 (2007) 13–28, doi: 10.1016/j.actamat.2006.07.008.
[36] Z.P. Luo, H.W. Zhang, N. Hansen, K. Lu, Quantification of the microstructures of high purity nickel subjected to dynamic plastic deformation, Acta Mater. 60 (2012) 1322–1333, doi: 10.1016/j.actamat.2011.11.035.
[37] M.A. Meyers, K.K. Chawla, Mechanical Behavior of Materials, Cambridge University Press, 2009.
[38] F. Yuan, P. Jiang, X. Wu, Annealing effect on the evolution of adiabatic shear band under dynamic shear loading in ultra-fine-grained iron, Int. J. Impact Eng. 50 (2012) 1–8, doi: 10.1016/j.ijimpeng.2012.07.001.
[39] A. Mishra, M. Martin, N.N. Thadhani, B.K. Kad, E.A. Kenik, M.A. Meyers, High-strain-rate response of ultra-fine-grained copper, Acta Mater. 56 (2008) 2770–2783, doi: 10.1016/j.actamat.2008.02.023.
[40] W. Chen, Z.S. You, N.R. Tao, Z.H. Jin, L. Lu, Mechanically-induced grain coarsening in gradient nano-grained copper, Acta Mater. 125 (2017) 255–264, doi: 10.1016/j.actamat.2016.12.006.
[41] K. Toshiro, Y. Isamu, N. Mitsuo, Evaluation of dynamic fracture toughness parameters by instrumented Charpy impact test, Eng. Fract. Mech. 24 (1986) 773–782, doi: 10.1016/0013-7944(86)90249-3.
[42] P.R. Sreenivasan, S.L. Mannan, Dynamic J-R curves and tension-impact properties of AISI 308 stainless steel weld, Int. J. Fract. 101 (2000) 229–249, doi: 10.1023/A:1007621904164.
[43] M.F. Ashby, Materials Selection in Mechanical Design, Butterworth-Heinemann, 2011.
[44] J.R. Rice, P.C. Paris, J.G. Merkle, Some further results of J-integral analysis and estimates, ASTM Spec. Tech. Publ. (1972) 231–245, doi: 10.1520/stp49643s.
[45] J.P. Tronskar, M.A. Mannan, M.O. Lai, Measurement of fracture initiation toughness and crack resistance in instrumented Charpy impact testing, Eng. Fract. Mech. 69 (2002) 321–338, doi: 10.1016/S0013-7944(01)00077-7.
[46] S.J. Garwood, J.N. Robinson, C.E. Turner, The measurement of crack growth resistance curves (R-curves) using the J integral, Int. J. Fract. 11 (1975) 528–530, doi: 10.1007/BF00033539.
[47] J.R. Rice, G.F. Rosengren, Plane strain deformation near a crack tip in a power-law hardening material, J. Mech. Phys. Solids 16 (1968) 1–12, doi: 10.1016/0022-5096(68)90013-6.

Please cite this article as: Y. Lin et al., On the impact toughness of gradient-structured metals, Acta Materialia (2020), https://doi.org/10.1016/j.actamat.2020.04.027